P1.1 USE OF SYNTHETIC APERTURE RADAR IN THE FINE-SCALE ANALYSIS OF SYNOPTIC-SCALE FRONTS AT SEA

Todd D. Sikora
United States Naval Academy, Annapolis, Maryland

George S. Young
Pennsylvania State University, University Park, Pennsylvania

Nathaniel S. Winstead
Johns Hopkins University Applied Physics Laboratory, Laurel, Maryland

1. INTRODUCTION

Fine-scale surface analysis of synoptic-scale weather systems is a challenging undertaking in the best of circumstances, but has proven particularly difficult at sea because of the paucity of in situ observations (Bosart 2003; Young et al. 1997). Remote sensing has taken a lead role in mitigating this problem. The success of remote sensing in this respect depends on the nature of the phenomena being analyzed, the quantity being measured by the remote sensor, and the ratio of the scales of interest to the spatial resolution of the remote sensor. For example, lower tropospheric streamline analysis via visible or infrared cloud track-winds would be problematic under cirrus overcast while a microwave scatterometer would face no such difficulty.

Synthetic aperture radar (SAR) offers particularly intriguing opportunities for improving the accuracy and resolution of marine surface analyses because of its ability to sense the ocean surface footprints of atmospheric processes, regardless of daylight and cloud conditions, and its order 10 m to 100 m spatial resolution (Sikora et al. 2004). Thus, SAR opens the possibility of conducting fine-scale surface analysis of marine weather systems, as Friedman et al. (2001) first demonstrated using polar mesoscale cyclones.

Here, we will focus on the use of SAR in the fine-scale analysis of synoptic-scale fronts, including the mesoscale and microscale substructure of the fronts. For clarity and compactness, we will invoke the scale nomenclature of Orlanski (1975). Therein, the spatial range of the macroscale is divided into α (i.e., planetary, 10,000 to 40,000 km) and β (i.e. synoptic, 2000 to 10,000 km). The mesoscale is divided into α (200 to 2000 km), β (20 to 200 km), and γ (2 to 20 km) and the microscale into α (200 to 2000 m), β (20 to 200 m), and γ (2 to 20 m). Of these, current spaceborne SAR instruments can fully observe only meso-β, meso-γ, and micro-α phenomena.

1.1 *Basics of Synthetic Aperture Radar*

As mentioned above, SAR senses the sea surface footprints of atmospheric phenomena. Typical SAR wavelengths are on the order of centimeters to decimeters. It follows then that there is little attenuation of the radar signal by the intervening atmosphere. Thus, the primary scatterers in SAR marine scenes are ocean surface waves forced by the near-surface wind. As wind speed increases, so does the wave amplitude at Bragg-resonant wavelength and, hence, SAR backscatter. Wind direction also affects the SAR backscatter. At moderate incident angles, a major maximum occurs when the wind is blowing opposite to the look direction of the radar and a minor maximum occurs when the wind is blowing in the same direction as the look direction of the radar. Minima occur when the wind blows perpendicular to the radar look direction. Thus, SAR-detected footprints reflect the fine-scale patterns in both wind speed and direction.

Because typical SARs have resolutions on the order of 10 m to 100 m and swath widths on the order of 100 km to 1000 km, they are ideal instruments for sensing the wind-driven sea surface signatures of various marine meteorological phenomena and thus for providing a basis for fine-scale marine meteorological analyses.

1.2 *Scope*

In this paper, we will demonstrate the viability of SAR as a tool for fine-scale marine meteorological analyses of synoptic-scale fronts using data from the Canadian Space Agency's RADARSAT-1. In particular, we will show how SAR can reveal the mesoscale and microscale sub-structures of synoptic-scale cold fronts, warm fronts, occluded fronts, and secluded fronts found over the Gulf of Alaska and off the east coast of North America.

These regions were examined because of the availability of a large number of RADARSAT-1 SAR images from the Alaska SAR Demonstration project. The SAR onboard RADARSAT-1 is C-band (5.6 cm) and right-looking with horizontal-horizontal polarization (HH-pol). RADARSAT-1 SAR has various sensor modes but the one employed herein is the ScanSAR wide mode has a swath width of approximately 500 km and has a resolution of 100 m. The data shown in this paper have been smoothed to 600 m resolution to eliminate speckle and to minimize the effect of ocean features. Of the 6000 Alaska SAR Demonstration Project images available for examination, approximately 90 percent were from the Gulf of Alaska and the Bering Sea with the remainder the east coast of North America between the east coast of Florida and New England. Examination of this Alaska SAR Demonstration Project dataset and the corresponding NOGAPS global analyses yielded 158 cases of well defined frontal signatures: 22 warm fronts, 37 cold fronts, 3 stationary fronts, 32 occluded fronts, and 64 secluded fronts. The latter are cases in which occluded fronts had wrapped around a low to form a closed seclusion. This frontal image collection forms the basis of the discussion below. All frequencies referred to therein are derived from this sample. For presentation purposes, all of the SAR imagery in this paper were processed to remove the strong incident angle trend present in HH-pol radar cross section (RCS) imagery. The resulting gray-scale images are related to backscatter and are hereafter referred to as SAR backscatter images. For each image, north is oriented towards the top of the page.

2. FRONTAL SIGNATURES IN SAR IMAGERY

Most synoptic-scale fronts share a number of SAR-observable features. The detection of these features in a SAR image thus provides evidence for the existence and location of a synoptic-scale front.

Often the first feature that catches an analyst's eye is a sharp (near zero-order) change in backscatter. This discontinuity is typically of at least meso-beta scale length, spanning most or all of a SAR image. In contrast, the width of the zone of strong backscatter gradient is much less, often meso-gamma to micro-alpha. The backscatter discontinuity signature in Figure 1 is typical of a

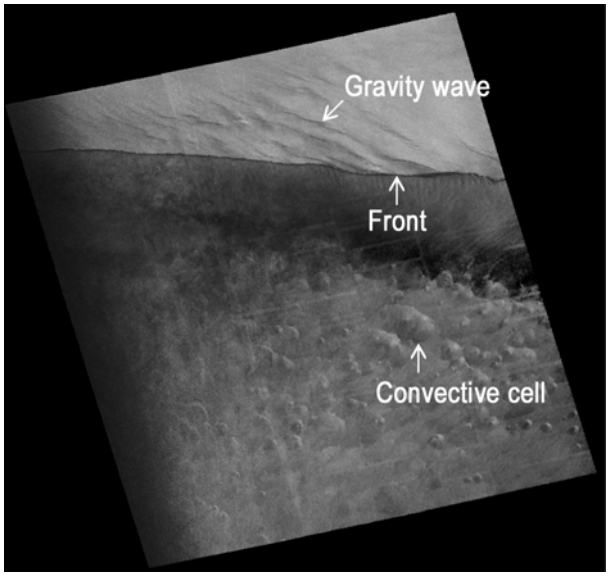

Figure 1. RADARSAT-1 synthetic aperture radar image of a well defined occluded front in the Gulf of Alaska, 3:20 UTC on January 12, 2003. Image is located at 53 N, 144 W.

well-defined synoptic-scale front, in this case an occluded front (frontal identification discussed below). This concentration of cross-frontal gradient is inherent in the frontogenetic process; a good working definition of a synoptic-scale front could, in fact, be "an elongated zone of significantly enhanced horizontal gradients of wind, temperature, or humidity resulting from deformation, shearing, tilting, or diabatic processes operating on the synoptic scale". Because frontogenesis concentrates horizontal gradients of the vector wind, there is generally a change in wind direction, and often wind speed, across a front. Depending on the wind-relative look angle of the SAR, these gradients will produce a corresponding gradient in backscatter, and hence the signature described above. It is possible, however, for these signatures to be masked when a chance combination of look angle and cross-front vector wind difference results in identical backscatter values for both sides of the front.

The same frontogenetic process that enhances vector wind gradients across fronts also concentrates the thermodynamic differences between adjacent air masses (Schultz et al. 1998). Thus there is typically a strong cross-frontal gradient in boundary layer temperature and a corresponding gradient in air-sea temperature difference (Neiman et al. 1990). If this stability change is sufficient to alter the type, scale, or

intensity of boundary layer turbulence, there can be a near zero-order change in the character of the micro-alpha to meso-gamma scale eddy signatures across the front. An intense cold front (frontal identification discussed below), such as that advancing eastward across Figure 2, will often

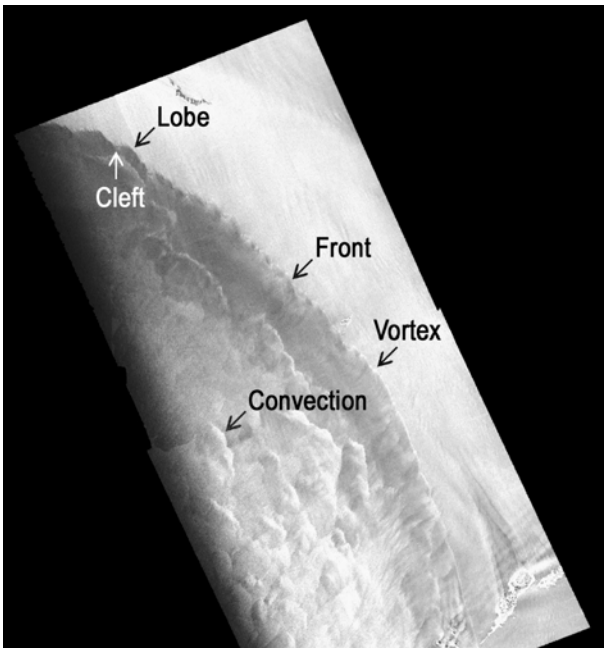

Figure 2. RADARSAT-1 synthetic aperture radar image of an intense cold front moving northeastward near the Aleutian Islands, 5:06 UTC on February 08, 2001. Image is located at 58 N, 172 W.

exhibit a clear-cut example of this signature, with a rather homogeneous backscatter pattern in the near-neutral-stratification atmosphere ahead of the front and strong modulation of backscatter by convective downdrafts in the more unstable boundary layer behind the front. The convective signatures often take the form seen here, with an arc-shaped leading gust fading to a trailing pool of lower wind speeds in a pattern reminiscent of that in downdraft-fed cold pools of much larger scale convective systems (Young et al. 1995). For the Alaska SAR Demonstration dataset, 30% of the cold fronts exhibited this signature while only 6 percent of the occluded fronts and none of the warm fronts did so. Thus, this signature appears to reflect the existence of strong cold advection in the immediate rear of the front.

The existence of a pre-frontal jet (Carlson 1980) can also contribute to the cross-frontal gradient in SAR backscatter, as captured in Figure 3 for a warm front (frontal identification discussed

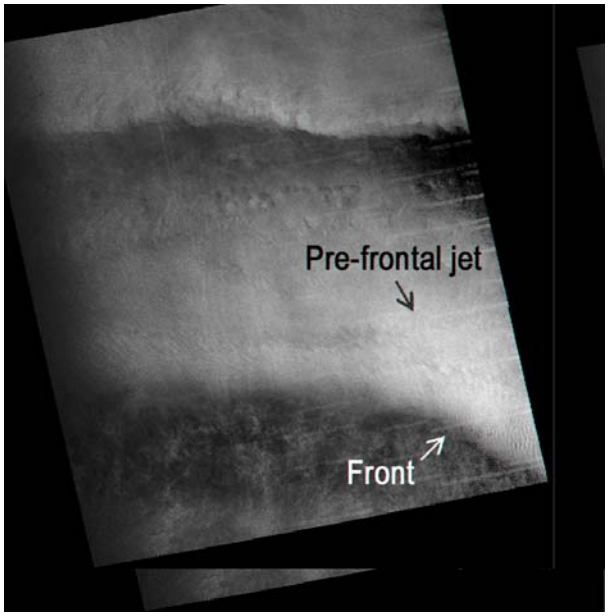

Figure 3. RADARSAT-1 synthetic aperture radar image of a warm front with pre-frontal jet to its north, Gulf of Alaska, 3:13 UTC on October 3, 2001. Image is located at 56 N, 143 W.

below), with higher backscatter ahead of the front than behind it. Pre-frontal jets with a pronounced maximum in backscatter paralleling the front were observed in 50 percent of the warm fronts, 31 percent of the occluded fronts, and only 10 percent of the cold fronts. The limited scale of SAR imagery may seriously impact these statistics, as may the high-latitude oceanic region from which most of the analyzed images came. Because of the frequency of cut-off lows in the Gulf of Alaska the most common form of pre-frontal jet is associated with a band of cloudiness extending north from the mid-latitudes and wrapping cyclonically around an occluded cyclone. In regions where traveling wave-cyclones dominate, pre-frontal jets in association with cold fronts (i.e., warm conveyor belts) become more common (Carlson 1980).

3. RECOGNIZING FRONTAL TYPES IN SAR IMAGERY

The subsequent sections will explore the SAR signatures that differ between frontal types, allowing the SAR analyst to contribute to identification of fronts by type. This discussion will be limited to cold, warm, occluded, and secluded fronts because stationary fronts were rare in the Alaska SAR Demonstration dataset. Access to SAR images from the subtropics would eliminate

this limitation and allow the extension of this analysis method to lower latitudes.

3.1 *Cold Fronts*

Because cold fronts advance as gravity currents (Young and Johnson 1984, Physick 1988), they often exhibit lobe and cleft instability (Lee and Wilhelmson 1997). The resulting bulges in the surface front, convex in the direction of frontal motion and cusped towards the cold air, can be seen in SAR images such as those in Figure 2. In the Gulf of Alaska, most fronts of this type advance from the northeast, out of the continental interior. Elsewhere in the northern hemisphere cold fronts more typically propagate out of the west or northwest. For the Alaska SAR Demonstration dataset 43 percent of cold fronts exhibit lobe and cleft instability as compared with 10 percent of other fronts. Thus, the existence of this bulge and cusp signature suggests that a frontal discontinuity is likely to be a cold front.

Another feature frequently observed in SAR imagery of cold fronts is the existence of a series of meso-gamma scale vortices spaced along the frontal discontinuity. The creation of these small-scale vortices along the leading edge of gravity currents is abetted by the clefts acting as initiation points for vortex wrap-up (Lee and Wilhelmson 1997; Parsons and Hobbs 1983), a process captured in Figure 2. Because cold fronts tend to exhibit a particularly narrow frontal zone and intense frontal lifting, a combination horizontal shear instability and stretching results in small but intense vortices. The resulting circulation intensity is often sufficient to saturate SAR imagery, as seen in Figure 2. These tightly wrapped vortices were observed only in cold fronts, and then only in about 1/3 of the cases. The most clear-cut examples are observed in the narrower fronts, but event and non-event cases could not be distinguished based on cross-frontal jump in backscatter, width of the frontal zone, or a shear index computed as the ratio of the two. The importance of vortex stretching in the dynamics behind this signature is reflected in the limited diagnostic power of these simple measures reflecting shear alone.

Some cold fronts also exhibit signatures associated with cross-frontal differences in boundary layer structure. Figure 2 provides particularly striking examples of meso-beta scale convective downdraft signatures behind a cold front. Only cold fronts were observed to exhibit these convective signatures immediately poleward of the front, and then only 13 percent of the time. That this result is regionally biased can be seen by considering the post-frontal stability for cold air outbreaks off the east coast of North America. The likelihood of convection could vary from near zero to almost 100 percent depending on season and thus the continent-ocean temperature difference (Young and Sikora 2003).

One of the rarest signatures of a cold front is a series of front-parallel meso-gamma scale backscatter bands resulting from Kelvin-Helmholtz instability behind the frontal head as seen in Figure 4 (Young and Johnson 1984). These front-parallel waves occur only when there is strong vertical shear of the cross-frontal wind component so they are endemic to fronts that behave as gravity currents, i.e., cold fronts and smaller-scale phenomena such as gust fronts and sea breezes. The signature is similar to that for an undular bore or a solitary wave packet (Alpers and Stilke 1996), therefore other factors must be considered when using this feature to diagnose frontal type.

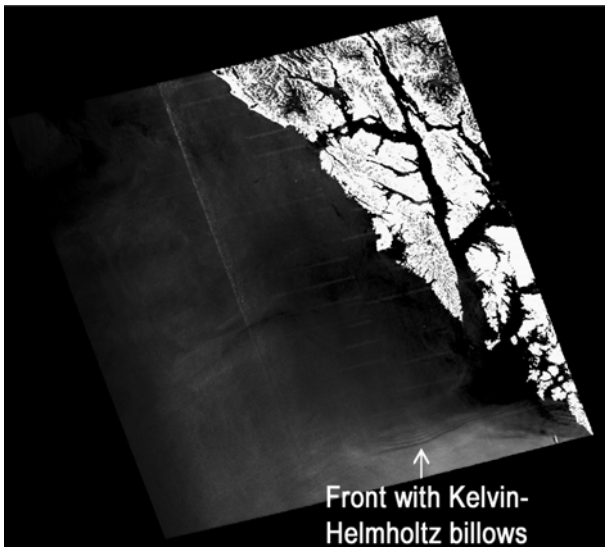

Figure 4. RADARSAT-1 synthetic aperture radar image of Kelvin-Helmholtz billows behind the head of a southward moving cold front off the Alexander Archipelago of southern Alaska, 2:48 UTC on May 25, 2002. Image is located at 56 N, 137 W.

3.2 *Warm Fronts*

Warm frontal boundaries (e.g., Figure 3) are typically much smoother than those of cold fronts, although they often meander in response to meso-beta scale vortices. Warm fronts exhibit waviness on this scale about 1/5 of the time, occluded fronts slightly less frequently, and cold fronts rarely.

Fronts that exhibit these vortices tend to be narrower than those without vortices but have similar cross-frontal differences in backscatter, suggesting that the cross-frontal shear is stronger. Thus, it is likely that these meso-beta scale frontal waves result from horizontal shear instability (Martin 1996).

Another signature of shear across the frontal zone is the existence of meso-gamma or micro-alpha scale banding aligned nearly perpendicular to the front (e.g., Figure 5). When present, such

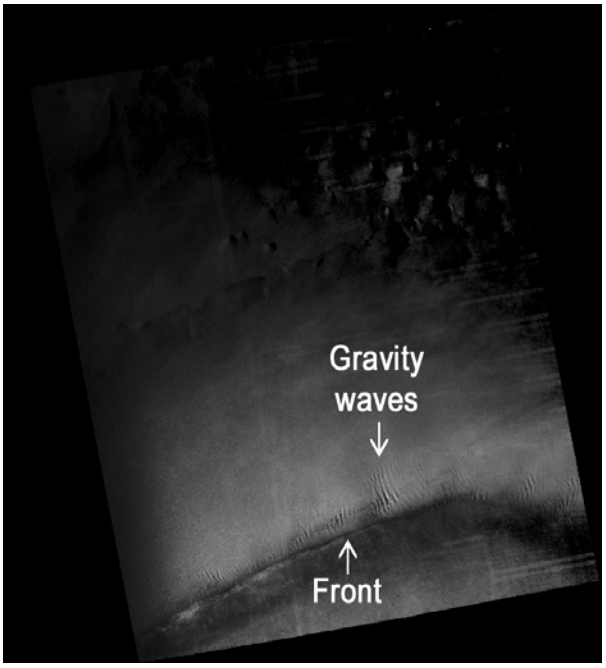

Figure 5. RADARSAT-1 synthetic aperture radar image of a warm front with gravity waves in the Gulf of Alaska, 3:20 UTC on March 30, 2002. Image is located at 53 N, 144 W.

bands usually extend only a few 10s of kilometers to the cold side of the front as in Figure 5. Given their smoothness and association with strong pre-frontal jets it is conjectured that they reflect shear-driven gravity waves in the frontal inversion. Similar signatures have been documented for terrain driven gravity waves in a frontal inversion, wherein they also faded as the frontal surface lifted further from the surface (Winstead et al 2002). Of potential dynamic interest is the apparent modulation of such gravity waves by horizontal shear instability waves as exhibited in Figure 5.

3.3 *Occluded Fronts*

Occluded fronts have many SAR-observable features in common with warm fronts, making them hard to distinguish on the basis of SAR imagery alone. As with warm fronts, occluded fronts are generally smooth except where they meander in response to meso-beta scale vortices. Moreover, front-perpendicular gravity wave signatures are also observed with some occluded fronts. Occasionally the gravity waves are oriented at more acute angles to the front as in Figure 1. Gravity wave signatures are about 50 percent (22 versus 14 percent) more common in occluded fronts than in warm fronts, perhaps reflecting the strong vertical shear associated with the pre-frontal jet wrapping into the major occluded cyclones of the Gulf of Alaska. One feature that can help distinguish occluded and warm fronts is the width of the backscatter gradient. This zone of changing wind speed and direction averages about twice as wide for the observed occluded fronts as for cold and warm fronts. Because the cross-front backscatter differences are similar for these three frontal types, it is possible that cross-front shear is weakest for occluded fronts. Combined with the indications that vertical shear is greatest in these fronts, this result is suggestive of differences in frontal slope. Such differences cannot, however, be verified without in situ upper air observations.

3.4 *Seccluded Fronts*

As occluded cyclones continue to evolve, the tip of the occluded front sometimes wraps into a ring leading to the seclusion stage of cyclone development (e.g. Chang et al. 1996; Kuo et al. 1992; Neiman and Shapiro 1993, Neiman et al. 1993). The resulting secluded front often has a surrounding low-level jet (an extension of the cold conveyor belt) with a tight radius of curvature (Figure 6). While existing theoretical and modeling studies suggest that the surface air in the center of these seclusions is warmer than that in the surrounding jet (e.g. Chang et al. 1996; Kuo et al. 1992), the NOGAPS global analysis sometimes indicates the existence of a cold core at the surface. Because there appears to be SAR-detectable differences between the warm-core and cold-core cases, they will be distinguished below and a SAR-supported conjecture about their origin will be presented. Thus, based on the NOGAPS-analyzed surface temperature field, seclusions will be divided into three categories: warm, cold, and indeterminate. Circum-seclusion jets with a notable fall-off in backscatter further out from the seclusion occur in 42 percent of warm seclusions,

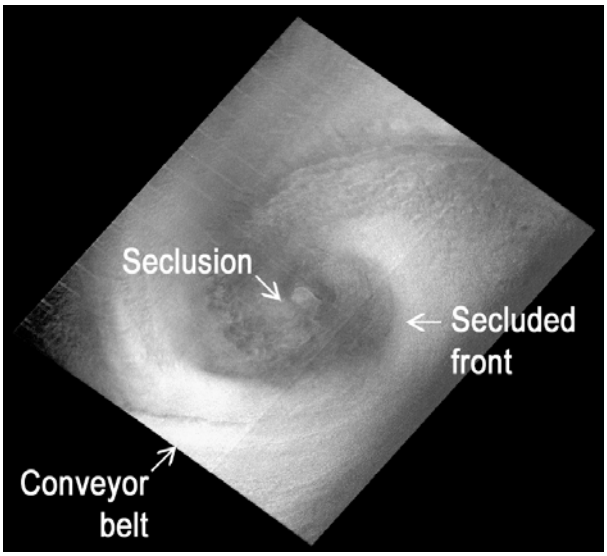

Figure 6. RADARSAT-1 synthetic aperture radar image of a secluded front in the Bering Sea, 18:18 UTC on December 16, 2000. Image is located at 55 N, 175 W.

36 percent of cold seclusions, and less than 33 percent of indeterminate seclusions. Thus, these jets are roughly as common as those ahead of warm fronts and occluded fronts. This result is in keeping with their formation as the downwind extension of a pre-existing cold conveyor belt (e.g. Kuo et al. 1992; Neiman and Shapiro 1993).

Occluded fronts also exhibit occasional cross-frontal differences in boundary layer signatures, but of a pattern more complex than that observed with cold fronts. Rather than the instability starting immediately poleward of the front, the onset of convective signatures is displaced 100 to 200 km, poleward in the case of a purely occluded front, radially outward in the case of a seclusion. This pattern was observed in 15 percent of warm seclusions, 11 percent of cold seclusions, 13 percent of indeterminate seclusions, and only 6 percent of un-secluded occluded fronts. In contrast, the pattern was not observed in association with warm fronts. It is conjectured that occluded or secluded fronts exhibiting this behavior are imbedded in the generally unstable environment of a cold-core cut-off low and further that it is the combination of low frontal inversion and warm advection in the trough of warm air aloft (Martin 1999) that prevents the formation of convective signatures in the 100 to 200 km closest to the front. Mesoscale modeling or in situ upper air observations would be required to verify this hypothesis.

Most seclusions have well defined backscatter fronts surrounding a low-wind core as seen in Figure 6. This backscatter gradient is often sharper in warm seclusions than in cold seclusions. Some 9 percent of warm seclusions exhibit mesoscale convective signatures within the low-wind core, cold seclusions have not been observed to do so. This difference suggests that the signatures are caused by convective mixing of air from the elevated cold core of the parent cut-off low with warm boundary-layer air trapped within the seclusion. Over time, this convective redistribution of heat could result in the extension of the cold core aloft to the surface replacing the advectively created warm core of the seclusion. It is hypothesized that this effect is responsible for the cold cores analyzed by NOGAPS for some seclusions, with the coldness of the mid levels being the deciding factor.

Seclusions differ from occluded fronts in that both warm and cold seclusions have about a 10 percent likelihood of exhibiting gravity wave signatures, about half that for other occluded fronts. Other features are however quite similar. Neither seclusions nor occlusions exhibit lobe and cleft instability and both have similar odds of exhibiting meso-beta scale waves (11 percent and 12 percent respectively).

4. CONCLUSIONS

Synthetic aperture radar imagery offers much better spatial resolution than other currently flying spaceborne remote sensors. SAR's resolution is an order of magnitude greater than that for operational cloud imaging satellites and two orders of magnitude greater than that for other surface wind imaging satellites. We argue that the inclusion of SAR into the marine analyst's toolbox would greatly facilitate the fine-scale analysis of atmospheric fronts at sea. The basis for this assertion comes from our analysis of some 6000 RADARSAT-1 SAR images from the Alaska SAR Demonstration data set. This analysis yielded 158 cases of well defined frontal signatures: 22 warm fronts, 37 cold fronts, 3 stationary fronts, 32 occluded fronts, and 64 secluded fronts. In the preceding discussion, we show how each category of front is distinguishable from the others, and we point out common SAR-observable fine-scale structure associated with each category of front.

Primary drawbacks to the operational use of SAR imagery in the preparation of fine-scale marine analyses are its limited cross-track spatial coverage in any one scene and its low frequency repeat cycle. These problems can be addressed

by the development of wide-swath SAR modes and the launch of more satellites bearing SARs. Until such time as additional wide-swath SARs join the constellation, SAR-based analyses serve primarily to provide insight into the structure and behavior of weather systems, information that that can subsequently be used to forecast the impacts of similar systems observed by other means. Issues addressable with the current generation of SAR data sets include the space and time climatology of the various sub-synoptic scale frontal structures discussed above, the relationship between these frontal structures and cloud features (using geosynchronous satellite cloud imagery), and possibly the discovery of new phenomena such as the near-front surface signatures of shear-driven gravity waves. These and equivalent studies of other marine meteorological phenomena require the widespread availability of SAR backscatter imagery, an issue that is contingent upon the data policy of those funding and administering SAR satellites.

5. ACKNOWLEDGMENTS

This work was supported by Office of Naval Research Grants N0001403WR20329, N0001404WR20365, and N00014040539. This work was also supported by National Science Foundation grant ATM-0240269 and ATM-0240869. This work benefited from valuable discussions with Peter Olsson of the Alaska Experimental Forecast Facility.

6. REFERENCES

Alpers, W., and G. Stilke, 1996: Observation of a nonlinear wave disturbance in the marine atmosphere by synthetic aperture radar aboard the ERS 1 satellite. *J. Geophys. Res.*, **101**, 6513-6525.

Beal, R. C., G. S. Young, F. Monaldo, D. Thompson, N. Winstead and C. Scott, 2003: High Resolution Wind Monitoring with Wide Swath SAR: A User's Guide. Available at http://fermi.jhuapl.edu/stormwatch/user_guide/

Bosart, L. F., 2003: Whither the weather analysis and forecasting process? *Wea. Forecasting*, **18**, 520-529.

Carlson, T. N., 1980: Airflow Through Midlatitude Cyclones and the Comma Cloud Pattern. *Mon. Wea. Rev*., **108**, 1498–1509.

Chang, S. W., T. R., Holt and K. D. Sashegyi, 1996: A Numerical Study of the ERICA IOP 4 Marine Cyclone. *Mon. Wea. Rev*., **124**, 27–46.

Friedman, K. S., T. D. Sikora, W. G. Pichel, P. Clemente-Colon and G. Hufford, 2001: Using spaceborne synthetic aperture radar to forecast polar mesoscale cyclones in the Bering Sea. *Wea. Forecasting*, **16**, 270-276.

Kuo, Y.-H., R. J. Reed and S. Low-Nam, 1992: Thermal Structure and Airflow in a Model Simulation of an Occluded Marine Cyclone. *Mon. Wea. Rev*., **120**, 2280–2297.

Lee, D. L., and R. B. Wilhelmson, 1997: The Numerical Simulation of Non-Supercell Tornadogenesis, Part I: Initiation and Evolution of Pretornadic Misocyclone Circulations along a Dry Outflow Boundary. *J. Atmos. Sci*., **54**, 32-60.

Martin, R. F., 1996: Observations of 250-km-Wavelength Clear-Air Eddies and 750-km-Wavelength Mesocyclones Associated with a Synoptic-Scale Midlatitude Cyclone *Mon. Wea. Rev*., **124**, 1199-1210

Martin, J. E., 1999: Quasigeostrophic Forcing of Ascent in the Occluded Sector of Cyclones and the Trowal Airstream. *Mon. Wea. Rev*., **127**, 70–88.

Neiman, P. J., and M. A. Shapiro, 1993: The Life Cycle of an Extratropical Marine Cyclone. Part I: Frontal-Cyclone Evolution and Thermodynamic Air-Sea Interaction. *Mon. Wea. Rev*., **121**, 2153–2176.

Neiman, P. J., Shapiro, M. A., E. G. Donall and C. W. Kreitzberg, 1990: Diabatic Modification of an Extratropical Marine Cyclone Warm Sector by Cold Underlying Water. *Mon. Wea. Rev*., **118**, 1576–1590.

Neiman, P. J., M. A. Shapiro and L. S. Fedor, 1993: The Life Cycle of an Extratropical Marine Cyclone. Part II: Mesoscale Structure and Diagnostics. *Mon. Wea. Rev*., **121**, 2177–2199.

Orlanski, I., 1975: A rationale subdivision of scales for atmospheric processes. *Bull. Amer. Meteor. Soc*., **56**, 527-530.

Parsons, D. B., and P. V., Hobbs, 1983: The Mesoscale and Microscale Structure and Organization of Clouds and Precipitation in Midlatitude Cyclones. XI: Comparisons between Observational and Theoretical Aspects of Rainbands. *J. Atmos. Sci.*, 40, 2377–2398.

Physick, W. L., 1988: Mesoscale Modeling of a Cold Front and Its Interaction with a Diurnally Heated Land Mass. *J. Atmos. Sci*., **45**, 3169–318

Schultz, D. M., D. Keyser and L. F. Bosart, 1998: The Effect of Large-Scale Flow on Low-Level Frontal Structure and Evolution in Midlatitude Cyclones. *Mon. Wea. Rev*., **126**, 1767–1791.

Sikora, T. D., G. S. Young, R. C. Beal, F. M. Monaldo and P. W. Vachon, 2004: Applications of synthetic aperture radar in marine meteorology. *Advances in Fluid Mechanics: Atmosphere - ocean surface interactions*, William Perrie, Ed., Wessex Institute of Technology, in press.

Sikora, T. D., G. S. Young, R. C. Beal and J. B. Edson, 1995: Use of spaceborne synthetic aperture radar imagery of the sea surface in detecting the presence and structure of the convective marine atmospheric boundary layer. *Mon. Wea. Rev*., **123**, 3623-3632.

Winstead, N. S., T. D. Sikora, D. R. Thompson and P. D. Mourad 2002: Direct influence of gravity waves on surface-layer stress during a cold air outbreak, as shown by synthetic aperture radar. *Mon. Wea. Rev.*, **130**, 2764-2776.

Young, G. S., J. A. Harlan and T. M. Georges, 1997: Application of over-the-horizon radar observations to synoptic and mesoanalysis over the Atlantic, *Wea. Forecasting*, **12**, 44-55.

Young, G. S., and R. H. Johnson, 1984: Meso- and microscale features of a Colorado cold front. *J. Climate Appl. Meteor*., **23**, 1315-1325.

Young, G. S., S. M. Perugini and C. W. Fairall, 1995: Convective wakes in the equatorial western Pacific during TOGA. *Mon. Wea. Rev*., **123**, 110-123.

Young, G. S., and T. D. Sikora, 2003: Mesoscale Stratocumulus Bands Caused by Gulf Stream Meanders. *Mon. Wea. Rev*., **131**, 2177–2191